On the combustion of fine iron particles beyond FeO stoichiometry: Insights gained from molecular dynamics simulations

L.C. Thijs[a,*], E. Kritikos[b], A. Giusti[b], W.J.S Ramaekers[a], J.A. van Oijen[a], L.P.H de Goey[a], X.C. Mi[a]

[a]*Department of Mechanical Engineering, Eindhoven University of Technology, P.O. Box 513, NL-5600 MB, Eindhoven, Netherlands*
[b]*Department of Mechanical Engineering, Imperial College London, London SW7 2AZ, United Kingdom*

Abstract

Molecular dynamics (MD) simulations are performed to investigate the thermal and mass accommodation coefficients (TAC and MAC, respectively) for the combination of iron(-oxide) and air. The obtained values of TAC and MAC are then used in a point-particle Knudsen model to investigate the effect on the combustion behavior of (fine) iron particles. The thermal accommodation for the interactions of Fe with N_2 and Fe_xO_y with O_2 is investigated for different surface temperature, while the mass accommodation coefficient for iron(-oxide) with oxygen is investigated for different initial oxidation stages Z_O, which represents the molar ratio of $O/(O + Fe)$, and different surface temperatures. The MAC decreases almost linearly as a function of Z_O, with a steeper slope when $Z_O < 0.5$ and a gentler slope when $0.5 < Z_O < 0.57$. By incorporating the MD-informed accommodation coefficients into the single iron particle model, the oxidation beyond $Z_O = 0.5$ (from stoichiometric FeO to Fe_3O_4) is modeled. A new temperature evolution for single iron particles is observed compared to results obtained with previously developed continuum models. Specifically, results of the present simulations show that the oxidation process continues after the particle reaching the peak temperature, while previous models predicting a maximum temperature was attained when the particle is fully oxidized to $Z_O = 0.5$. Since the rate of formation slows down as the MAC decreases with an increasing oxidation stage, the rate of heat loss exceeds the rate of heat release upon reaching the maximum temperature. Finally, the effect of transition-regime heat and mass transfer on the combustion behavior of fine iron particles is investigated and discussed.

Keywords: Iron particle; Knudsen transition heat and mass transfer; Thermal accommodation coefficient; Mass accommodation coefficient; Molecular dynamics; Metal combustion; Metal-enabled cycle of renewable energy

1. Introduction

   Iron powder is considered as a promising metal fuel since it is inherently carbon-free, recyclable, compact, cheap and widely available (Bergthorson et al., 2015). To design and improve real-world iron-fuel burners, an in-depth understanding of the fundamentals underlying the combustion of fine iron particles is required.

   Over the past five years, the interest in using iron powder as a circular carrier of renewable energy has drastically increased. Soo et al. (2017), Tang et al. (2009), McRae et al. (2019), Tóth et al. (2020) and Li et al. (2021) performed experiments with iron dust flames to study fundamental characteristics of iron combustion, such as flame structure and flame propagation. Tóth et al. (2020) and Li et al. (2021) identified the formation of nano-particles in their experiments, where they observed halos of nano-particles surrounding the burning iron particles. To gain a more in-depth understanding of the oxidation processes of iron particles, the canonical configuration of single iron particle combustion has been investigated by multiple researchers. Ning et al. (2021a,b) performed single particle combustion experiments where the particles are ignited by a laser. They showed that the duration of burning process is sensitive to the surrounding oxygen concentration. They also observed that the maximum particle temperature increases with gas-phase oxygen concentration while reaching a plateau at sufficiently elevated oxygen concentrations. Formation of

oxide nano-particles during the combustion was also recorded. Li et al. (2022) investigated the ignition and combustion process of single micron-sized iron particles in the hot gas flow of a burned methane-oxygen-nitrogen mixture, and drew similar conclusions as Ning et al. (2021a). Panahi et al. (2022) used a drop-tube furnace to burn iron particles at a high gas temperature ($\approx$ 1350 K) with oxygen concentrations of 21%, 50% and 100%. They showed that particle temperature increases significantly when the oxygen concentration increases from 21% to 50%, but barely further increases when increasing from 50% to 100%.

In the past few years, the number of theoretical models for single iron particles has increased. Mi et al. (2022) investigated the ignition behavior of iron particles via solid-phase oxidation kinetics described by a parabolic rate. Jean-Philyppe et al. (2022) extended this model and investigated the ignition behavior of fine iron particles in the Knudsen transition regime. They stated that the transition effect on the ignition characteristics becomes important if the particle diameter is below 30 μm. Senyurt and Dreizin (2022) studied the ignition of metal particles other than iron in the transition regime, and stated that transition effects could always be neglected for very large (i.e., > 200 μm) particles. While these models only focused on the ignition, Soo et al. (2018) developed a generic model for the full combustion behavior for non-volatile solid-fuel particles, wherein the particle oxidation rate depends on reaction kinetics at the surface of the particle and the external diffusion of oxygen to the particle. Hazenberg and van Oijen (2021) further extended this model by taking into account the growth of the particle during oxidation. In Thijs et al. (2023), a boundary layer resolved model was developed so that mass and heat transfer are accurately modeled, including Stefan flow. Temperature-dependent properties were used for the gas- and condensed-phase species and evaporation was implemented to investigate the formation of nano-sized iron-oxides products. It was shown that, although the particle temperature remains below the boiling point of iron(-oxide), a non-negligible amount of iron mass is lost due to the evaporation of the particle. Furthermore, it was shown that when only the conversion of Fe to FeO is considered up to the maximum temperature, and when internal transport is neglected, a good agreement was obtained with the experimental data of (Ning et al., 2021b) for the combustion time and maximum temperature as a function of oxygen concentration. The further oxidation after the particle peak temperature was, however, not modeled. In a later work of (Thijs et al., 2022), the point-particle model of Hazenberg and van Oijen (2021) was extended, with aid of a boundary-layer-resolved model, to include temperature-dependent properties, slip velocity, Stefan flow, and evaporation.

In most of the previously discussed models for iron-particle combustion, the continuum assumption is used to describe the transport processes. It is known that, when the size of the particle becomes too small, modeling the heat and mass transfer using the continuum approach becomes invalid. The particle radius, r_p, compared to the mean free path length of the gas molecules, λ_{MFP}, is described by the Knudsen number (Liu et al., 2006)

$$Kn = \lambda_{MFP}/r_p. \tag{1}$$

Typically, when Kn is larger than 0.01 (Liu et al., 2006), the continuum approach is invalid. An elaborate review of modeling heat transfer in the transition regime for nano-particles in the context of laser-induced incandescence is presented by Liu et al. (2006). In the previous study of Thijs et al. (2023), only relatively large particles of 40 and 50 μm were considered, ensuring that the transition-regime heat and mass transfer has a negligible effect. While Jean-Philyppe et al. (2022) and Senyurt and Dreizin (2022) studied the transition effect on the ignition behavior of metal particles, such a study was not performed for the complete combustion process of single iron particles.

The heat and mass transfer in the free-molecular regime is dependent on the thermal and mass accommodation coefficients. The average energy transfer when gas molecules scatter from the surface is described by the thermal accommodation coefficient (TAC). The mass accommodation coefficient (MAC) or absorption coefficient is defined as the fraction of incoming oxygen molecules that are absorbed (accommodated) rather than reflected when they collide with the iron surface. Molecular dynamics simulation can be used to investigate these accommodation coefficients. Multiple authors (Daun, 2009, Daun et al., 2012, Sipkens et al., 2014, Sipkens and Daun, 2018) performed molecular beam simulations between metal-gas surfaces to investigate the TAC under different conditions. Daun et al. (2012) showed that the TAC obtained with such a molecular dynamics simulation well agrees with experimental data. Alas, to the authors' knowledge, a systematic analysis of the TAC and MAC for a system of iron(-oxide) surface exposed to air has not yet been reported. Such a study of the MAC is also of importance to derive effective chemical kinetics governing the rate of further oxidation beyond the stoichiometry of FeO, which are missing in literature.

In this work, molecular dynamics simulations are performed to determine the TAC and MAC for an iron(-oxide)-air system. Then, these values are used to examine the effect of the Knudsen transition regime on the combustion

behavior of single iron particles. The paper is organized as follows. Section 2 describes the methodology of the boundary-sphere model used to describe the combustion of single iron particles. In Section 3 the procedure for the molecular dynamics simulations is discussed. Section 4 presents the results of the molecular dynamics simulations. In Section 5 the results of the single iron particle model are discussed. Conclusions are provided in Section 6.

2. Model formulation for single iron particle combustion

In the current study, a two-layer point-particle model is used as shown in Figure 1. An iron particle oxidation model is coupled to a boundary sphere method to take into account the Knudsen transition regime. The iron particle oxidation model is based on the previous work (Thijs et al., 2022).
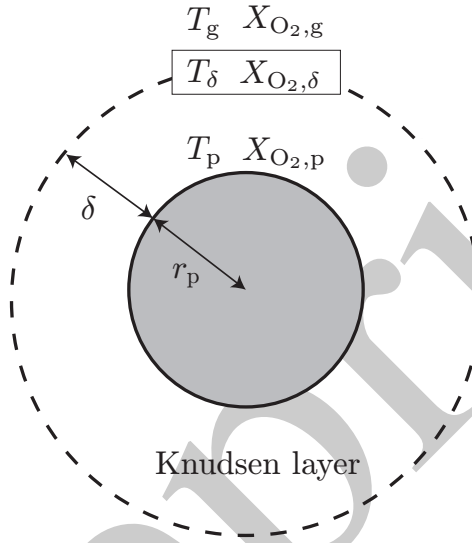

Figure 1: The configuration for heat and mass transfer analysis considered in the Knudsen model.

In Thijs et al. (2022), only the oxidation from Fe into FeO was taken into account via

$$R1 : Fe + \frac{1}{2}O_2 \rightarrow FeO. \tag{2}$$

Here, the oxidation mechanism is extended by considering the further oxidation into Fe_3O_4. Once all the Fe is converted into FeO, the FeO continues to oxidize into Fe_3O_4 via

$$R2 : 3FeO + \frac{1}{2}O_2 \rightarrow Fe_3O_4. \tag{3}$$

Based on the thermodynamics of the Fe-O system (Wriedt, 1991), it is known that iron-oxide can be formed in multiple crystalline structures, i.e., FeO (wustite), Fe_3O_4 (magnetite), and Fe_2O_3 (hematite). In the liquid phase of an Fe-O mixture, there are no clear crystalline structures. This region on the Fe-O phase diagram consists mainly of two different liquids denoted by L1 (iron) and L2 (iron-oxide). Therefore, considering these phases as "liquid FeO" and "liquid Fe_3O_4" is not in line with the phase diagram.

The thermodynamic data for the L1 and L2 mixture are, however, unknown. In this work, the thermodynamic data for the L1 and L2 mixtures are therefore approximated to be a linear combination of the liquid-phase data of Fe, FeO, and Fe_3O_4. The total enthalpy of a liquid iron particle, $H_{liq,tot}$, is determined via

$$H_{liq,tot} = m_{Fe}h_{Fe} + m_{FeO}h_{FeO} + m_{Fe_3O_4}h_{Fe_3O_4}, \tag{4}$$

with, m_i the mass of species i in the particle and h_i the mass specific enthalpy of species i (calculated with the NASA polynomials). This method was also used in the previous studies (Thijs et al., 2022, 2023).

3

The phase diagram of the Fe-O system is dependent on the molar ratio of O/ (O + Fe), which defines the oxidation stage of the (liquid) iron particle. Here, this ratio is denoted by Z_O, which is the elemental mole fraction of oxygen in the particle, and is defined as

$$Z_O = \frac{m_{O,p}/M_O}{m_{Fe,p}/M_{Fe} + m_{O,p}M_{Fe}}, \tag{5}$$

where $m_{O,p}$ is the mass of oxygen, $m_{Fe,p}$ the total mass of iron in the particle, and M_O and M_{Fe} are the molar mass of oxygen and iron, respectively. In this work, Z_O denotes the oxidation stage of the iron particle, where $Z_O = 0.5$ represents "liquid FeO" and $Z_O = 0.57$ "liquid Fe$_3$O$_4$".

To calculate the total enthalpy of the particle, the rates of change of m_{Fe}, m_{FeO}, and $m_{Fe_3O_4}$ need to be tracked. Since the vapor pressure calculated with the thermodynamic data of liquid Fe$_3$O$_4$ is orders-of-magnitude lower than those of liquid Fe and FeO (Ning et al., 2021b), evaporation of Fe$_3$O$_4$ is negligible compared to the evaporation of Fe and FeO. The rate of change of m_{Fe}, m_{FeO}, and $m_{Fe_3O_4}$ are related to the rate of oxidation and the rate of evaporation via

$$\frac{dm_{Fe}}{dt} = -\frac{1}{s_{Fe,1}}\dot{m}_{O_2,1} - \frac{dm_{evap,Fe}}{dt}, \tag{6}$$

$$\frac{dm_{FeO}}{dt} = -\frac{1}{s_{FeO,1}}\dot{m}_{O_2,1} - \frac{1}{s_{FeO,2}}\dot{m}_{O_2,2} - \frac{dm_{evap,FeO}}{dt}, \tag{7}$$

$$\frac{dm_{Fe_3O_4}}{dt} = -\frac{1}{s_{Fe_3O_4,2}}\dot{m}_{O_2,2}, \tag{8}$$

with $\dot{m}_{O_2,j}$ the mass transfer rate of oxygen to the particle via either reaction R1 (denoted by 1) or R2 (denoted by 2) and $s_{i,j}$ is the stoichiometric mass ratio of species i for reaction j. The total mass transfer rate of oxygen is given by $\dot{m}_{O_2} = \dot{m}_{O_2,1} + \dot{m}_{O_2,2}$. Note that R1 and R2 are sequential reactions in this work.

To calculate Z_O, the mass of O and Fe in the particle must be known. The rate of changes of O is related to the rate of oxidation and the rate of evaporation of FeO, while the rate of change of m_{Fe} which is in the particle, is only affected by evaporation

$$\frac{dm_{O,p}}{dt} = \dot{m}_{O_2} - \frac{M_O}{M_{FeO}}\frac{dm_{evap,FeO}}{dt}, \tag{9}$$

$$\frac{dm_{Fe,p}}{dt} = -\frac{dm_{evap,Fe}}{dt} - \frac{M_{Fe}}{M_{FeO}}\frac{dm_{evap,FeO}}{dt}, \tag{10}$$

with M_{FeO} the molar mass of FeO. Temperature-dependent density functions are used to relate the mass of the particle to the volume and diameter, see van Gool et al. (2022) for the specific polynomials.

The rate of change of the particle enthalpy is described by

$$\frac{dH_p}{dt} = q + q_{rad} + \dot{m}_{O_2}h_{O_2} - \sum_i h_{i,v}\frac{dm_{evap,i}}{dt}, \tag{11}$$

with q the heat transfer rate, q_{rad} the radiative heat transfer rate, h_{O_2} the mass-specific enthalpy of the consumed oxygen and $h_{i,v}$ the mass-specific enthalpy of the evaporated species.

To model the mass transfer rate $\dot{m}_{O_2}$ and heat transfer rate q, a boundary sphere method is used. Figure 1 illustrates the configuration which is used for the boundary sphere method. The iron particle is surrounded by a spherical Knudsen layer δ with a thickness equal to the mean free path λ_{MFP} of the gas molecules (Liu et al., 2006)

$$\lambda_{MFP} = \frac{k_\delta}{p}\frac{\gamma_\delta - 1}{9\gamma_\delta - 5}\sqrt{\frac{8\pi m_{O_2}T_\delta}{k_b}}, \tag{12}$$

with k_δ and γ_δ being the thermal conductivity and specific heat ratio derived at the Knudsen layer, p the ambient pressure, m_{O_2} the mass of an oxygen molecule, and k_b the Boltzmann constant.

At the Knudsen layer, the gas has a temperature T_δ and mole fraction X_δ. In the boundary sphere method, it is assumed that the heat and mass transfer across the Knudsen layer is quasi-steady (Liu et al., 2006). Therefore, the

4

mass balance at $r = \delta$ yields $\dot{m}_{O_2,FM} = \dot{m}_{O_2,c}$, with $\dot{m}_{O_2,FM}$ the mass transfer rate in the free-molecular regime and $\dot{m}_{O_2,c}$ the mass transfer rate in the continuum regime. Similarly, the heat balance can be written as $q_{FM} = q_c$.

The mass transfer rate and heat transfer rate in the continuum regime can be described as (Thijs et al., 2022, Senyurt and Dreizin, 2022)

$$\dot{m}_{O_2,c} = 2\pi Sh\left(\delta + r_p\right)\rho_{O2,f}D_f\left(X_{O_2,\delta} - X_{O_2,g}\right), \tag{13}$$

$$q_c = 2\pi Nu\left(\delta + r_p\right)k_f\left(T_\delta - T_g\right), \tag{14}$$

with $\rho_{O2,f}$, D_f and k_f the density of oxygen, the mixture-averaged diffusion coefficient and the thermal conductivity derived at 1/2-film temperature and composition (Thijs et al., 2022). T_g is the gas temperature, $X_{O_2,g}$ the mole fraction of oxygen in the gas phase, and Nu and Sh the Nusselt and Sherwood numbers, respectively. Here, ρ_{O_2} is defined as

$$\rho_{O_2} = \frac{M_{O_2}p}{R_u T}, \tag{15}$$

with M_{O2} the molar mass of oxygen and R_u the universal gas constant. A constant slip velocity is assumed, and the Stefan flow correction for the Nusselt and Sherwood numbers is incorporated. For more details of the continuum model, the reader is referred to Thijs et al. (2022).

The mass transfer rate in the free-molecular regime can be described as (Senyurt and Dreizin, 2022)

$$\dot{m}_{O_2,FM} = \alpha_m \pi r_p^2 v_\delta \rho_{O2,\delta} X_{O_2,\delta}, \tag{16}$$

with α_m the mass accommodation coefficient and v_δ the velocity of the gas molecules calculated as

$$v_\delta = \sqrt{\frac{8k_b T_\delta}{\pi m_{O_2}}}. \tag{17}$$

Similarly, the heat transfer rate in the free-molecular regime yields (Liu et al., 2006)

$$q_{FM} = \alpha_T \pi r_p^2 p \sqrt{\frac{k_b T_\delta}{8\pi m_{O_2}}} \frac{\gamma^* + 1}{\gamma^* - 1}\left(\frac{T_p}{T_\delta} - 1\right), \tag{18}$$

with α_T the thermal accommodation coefficient and γ^* the averaged specific heat ratio (Liu et al., 2006). It is assumed that the slip velocity and Stefan flow do not affect the free-molecular transport and the effect of the transition regime on the evaporation rate is neglected.

The boundary sphere method is implicit—a coupled system of nonlinear equations must be solved to find the mass and heat transfer rates. The molar fraction of oxygen $X_{O_2,g}$ and the temperature T_g in the gas phase are known. Therefore, $X_{O_2,\delta}$ and T_δ remain unknown and should be found via an iterative method. In this work, the lsqnonlin method of MATLAB was used to solve the coupled system of nonlinear equations. The Cantera toolbox was used to calculate the transport properties in the gas phase.

3. Model formulation for molecular dynamics simulations

Molecular beam simulations, where a large number of independent scattering events between a single gas molecule and a surface are simulated, are performed (Sipkens and Daun, 2018) to determine the TAC and MAC. For the interaction of N_2 with an iron surface, no chemical absorption is expected. Furthermore, to the authors' knowledge, there is no reactive force field available in the literature for an Fe-O-N system. Therefore, only a TAC value for the nitrogen molecule in combination with an iron surface is determined. As a result, the Fe-N_2 interactions are modeled using non-reactive potentials. On the contrary, reactive molecular dynamics are considered for the Fe_xO_y-O_2 interactions, to compute the TAC and MAC. Large-scale Atomic/Molecular Massively Parallel Simulator (LAMMPS) (Thompson et al., 2022) is used to perform the molecular dynamics simulations.

3.1. Thermal and mass accommodation coefficients

As previously described, the free-molecular heat transfer rate is dependent on the TAC. The TAC describes the average energy transfer when gas molecules scatter from the surface and is defined as

$$\alpha_{\mathrm{T}} = \frac{\langle E_0 - E_i \rangle}{3k_{\mathrm{B}}\left(T_{\mathrm{s}} - T_{\mathrm{g}}\right)}, \tag{19}$$

with $\langle \cdot \rangle$ denoting an ensemble average, E_0 the total energy of the scattered molecule, and E_i the energy of the incident molecule. The denominator represents the maximum energy that could be transferred from the surface to the gas molecule, with T_{s} the surface temperature and T_{g} the gas temperature.

The free-molecular mass transfer rate is dependent on the MAC. The MAC or absorption coefficient is defined as the fraction of incoming oxygen molecules that, upon collision with the iron surface, are absorbed (accommodated) rather than reflected. The MAC is defined as

$$\alpha_{\mathrm{m}} = \frac{n_{\mathrm{abs,g}}}{n_{\mathrm{tot,g}}}, \tag{20}$$

with $n_{\mathrm{abs,g}}$ the number of absorbed gas molecules and $n_{\mathrm{tot,g}}$ the total number of gas molecules colliding the surface.

When iron is burned in air, both oxygen and nitrogen may contribute to the total TAC. The MAC determines the contribution of oxygen to total TAC. In this work, the total TAC is calculated as

$$\alpha_{\mathrm{T,tot}} = \left[1 - X_{\mathrm{O_2}}\left(1 - \alpha_{\mathrm{m}}\right)\right]\alpha_{\mathrm{T,N_2}} + X_{\mathrm{O_2}}\left(1 - \alpha_{\mathrm{m}}\right)\alpha_{\mathrm{T,O_2}}. \tag{21}$$

3.2. Fe - N_2 interaction

To determine the thermal accommodation coefficients, the procedure as performed by Sipkens and Daun (2018) is followed. Figure 2 shows the initial configuration used to determine the thermal accommodation coefficient of the Fe-N_2 system. A molecular system is defined with a surface of 686 iron atoms initially arranged in a body-centered cubic (BCC) lattice, with a lattice constant of 2.856 Å, and a nitrogen molecule, of which the latter is modeled as a rigid rotor. The gas molecule is positioned around 10 Å above the surface, beyond the range of the potential well. In order to represent a specific surface temperature, a heating process is required for the iron surface to increase the kinetic energy of the system. Yan et al. (2017) showed that the phase change temperature obtained with MD simulations depends on the used heating process. Therefore, if the surface is expected to be in a solid phase, the surfaces are heated for 30 ps using the canonical (NVT) ensemble. To keep a constant temperature in the NVT ensemble simulations, the Nose-Hoover thermostat is applied on the translational degrees of freedom of the atoms with a temperature damping period of 100 fs. The warmed surfaces are then allowed to run first in the NVT ensemble and then in the micro-canonical (NVE) ensemble for 5 ps after which their state is saved to a file. If the surface is expected to be in a liquid phase, the surfaces are warmed using the Nose-Hoover thermostat for 30 ps to 2800 K, equilibrated for 5 ps at 2800 K and then gradually cooled down to the target temperature within 10 ps. Six different surfaces, each with different initial velocities, are generated to obtain a statistically meaningful set of data. Then, incident gas molecules are introduced with their velocities sampled from the Maxwell-Boltzmann (MB) distribution. 500 cases per warmed surface are sampled, which results in 3000 data points per configuration. The equations of motion are advanced using the Verlet algorithm with a timestep of 1 fs.

The interactions between the iron atoms are modeled using the embedded atom method (EAM) potential. The EAM force fields are based on the principle of embedding atoms within an electron cloud. The EAM potential reads

$$U_i = \frac{1}{2}\sum_{j \neq i} U_2\left(r_{ij}\right) - F\left(\sum_{j \neq i} \rho_j\left(r_{ij}\right)\right), \tag{22}$$

where U_2 is a pairwise potential between atoms i and j, r_{ij} is the distance between atoms i and j, F is the embedding function, and ρ_j is the contribution to the electron charge density from atom j. Sipkens and Daun (2018) investigated the effect of different surface potentials on the characteristics of an iron lattice, and found that the EAM potential of Zhou et al. (2004) is the most robust choice since this potential well predicts the phase transitions and experimentally measured densities. Therefore, this work uses the EAM potential of Zhou et al. (2004) for the iron surface potentials.
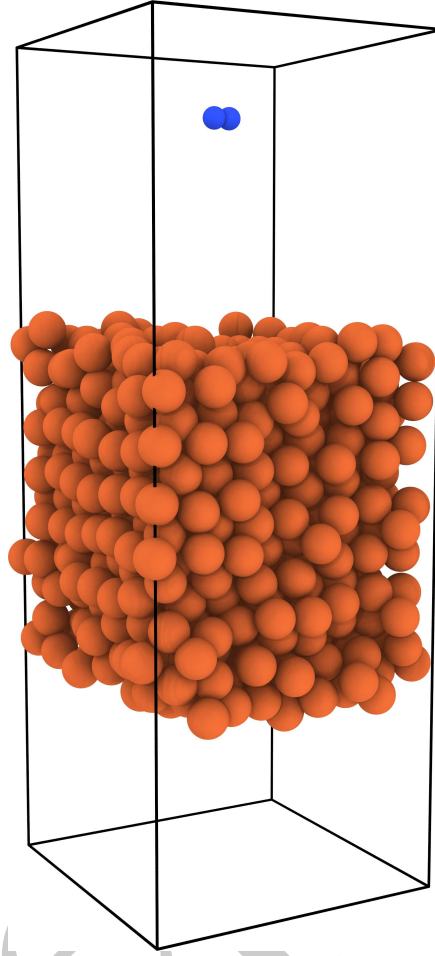
Figure 2: Initial configuration showing a nitrogen molecule (blue particles) placed above an iron surface (brown particles), with $Z_O = 0$ and $T_p = 2000$ K. The size of the particles equal the atomic radii.

The most used gas-surface pairwise potentials are the Lennard-Jones (LJ) 6-12 potential and the Morse potential. The LJ potential reads

$$U_{ij} = 4D_0 \left[\left(\frac{\sigma}{r_{ij}} \right)^{12} - \left(\frac{\sigma}{r_{ij}} \right)^6 \right], \tag{23}$$

where D_0 is the well depth, and σ is the distance at which U_{ij} is zero. The Morse potential reads

$$U_{ij} = D_0 \left(1 - e^{-\alpha(r-r_0)} \right)^2, \tag{24}$$

where r_0 is the equilibrium bond distance and α controls the width of the potential.

Daun et al. (2012) demonstrated the significance of using a well-defined gas-surface potential. They compared the TAC calculated with a Lennard-Jones 6-12 gas-surface potential with parameters derived from the Lorentz-Berthelot (LB) combination rules to the TAC calculated with a Morse potential with parameters derived from *ab initio* technique. For the LJ potential with LB combination rules, the well depth D_0 and finite distance σ were calculated by combining these values of the two individual atoms. For the *ab initio* calculations a molecule was moved towards a surface and then the potential was calculated from first principles. Daun et al. (2012) showed that the TAC is overestimated when using a Lennard-Jones 6-12 gas-surface potential with parameters derived from the Lorentz-Berthelot (LB) combination rules, but found a good agreement with the values obtained from experiments when using a Morse

potential with parameters derived from *ab initio* technique. The *ab initio* calculations for the Fe - N_2 interaction were performed by Sipkens et al. (2014). They found $D_0 = 2.162$ meV, $\alpha = 0.932$ Å^{-1} and $r_0 = 4.819$ Å.

3.3. Fe$_x$O$_y$ - O$_2$ interaction

Different iron-oxide surfaces will be generated to investigate the effect of the oxidation stage of the iron-oxide surface on the TAC and MAC. The surface oxidation stage is denoted by the elemental mole fraction of oxygen in the particle and can be calculated as

$$Z_O = \frac{n_{O,s}}{n_{tot,s}}, \tag{25}$$

with $n_{O,s}$ being the number of oxygen atoms and $n_{tot,s}$ the total number of atoms in the surface.

Before applying the Nose-Hoover thermostats, an FeO lattice is deposited in a specific ratio on top of a BCC lattice of Fe atoms. An initial distance of 4Å between the two layers is introduced to ensure a natural mixing. The height of the FeO lattice compared to the Fe lattice is increased to increase the Z_O of the specific surface. Two different heating strategies are used to investigate the effect of the distribution of oxygen atoms over the surface:

1. The same heating strategy previously discussed for the Fe surface is used, with a different heating strategy for a solid or liquid surface.
2. An annealing process is employed for all the surfaces to enhance the mixing of the O and Fe atoms. The surfaces are warmed using the Nose-Hoover thermostat for 30 ps to 2800 K, equilibrated for 30 ps at 2800 K and then gradually cooled down to the target temperature within 30 ps.

Figure 3 shows the preparation of an iron-oxide surface with $Z_O = 0.11$ and $T_p = 2000$ K via heating strategy 1. After the surface realization, an O_2 molecule is located around 10 Å above the surface, beyond the range of the potential well. Figure 4 shows the initial configuration used for the interaction between Fe$_x$O$_y$ and O_2.

Reactive molecular dynamics is used to simulate the interaction between Fe$_x$O$_y$-O_2. Reactive MD uses reactive force fields to accurately describe bond formation and breaking. ReaxFF (van Duin et al., 2001) is a bond order potential that describes the total energy of the system as

$$\begin{aligned} E_{system} &= E_{bond} + E_{over} + E_{under} + E_{val} + E_{tor} \\ &\quad + E_{vdWaals} + E_{Coulomb} + E_{additional}, \end{aligned} \tag{26}$$

with E_{bond} the bond formation/breaking energy, E_{over} and E_{under} the over- and undercoordination energy penalties, E_{val} and E_{tor} are respectively the valence and torsion angle energies, $E_{vdWaals}$ and $E_{Coulomb}$ are the non-bonded van der Waals and Coulomb long-range interactions and $E_{additional}$ are additional correction terms. The atomic charges are computed at every timestep using the charge equilibration method. A time step of 0.1 fs is used, which is recommended for reactive MD simulations at high temperatures (Kritikos et al., 2022). The timestep is held sufficiently small to capture all reaction events at high temperatures.

4. Results of the molecular dynamics simulations

Results from MD simulations are discussed below. First, the effect of the available reactive force fields is investigated by examining the predicted thermal expansion. Then, the mass and thermal accommodation coefficients are determined. It is of importance to note that the findings might be limited by the available (reactive) force fields, and could therefore change if different force fields are used.

4.1. Effect of reactive force field on iron oxide surface

Two different reactive force fields for Fe-O interactions, which are available in the literature, are compared. The ReaxFF FeOCHCl − 2010 (Aryanpour et al., 2010) is compared with the ReaxFF FeCHO − 2016 (Islam et al., 2016). The reactive force field (ReaxFF FeOCHCl − 2010) proposed by Aryanpour et al. (2010) was developed for Iron-Oxyhydroxide Systems. Islam et al. (2016) merged the ReaxFF force field for an Fe-C-H system (Zou et al., 2012) with the latest ReaxFF carbon parameters of Srinivasan et al. (2015). They developed their reactive force field to mainly study the interaction of hydrogen with pure and defective ferrite-cementite interfaces.
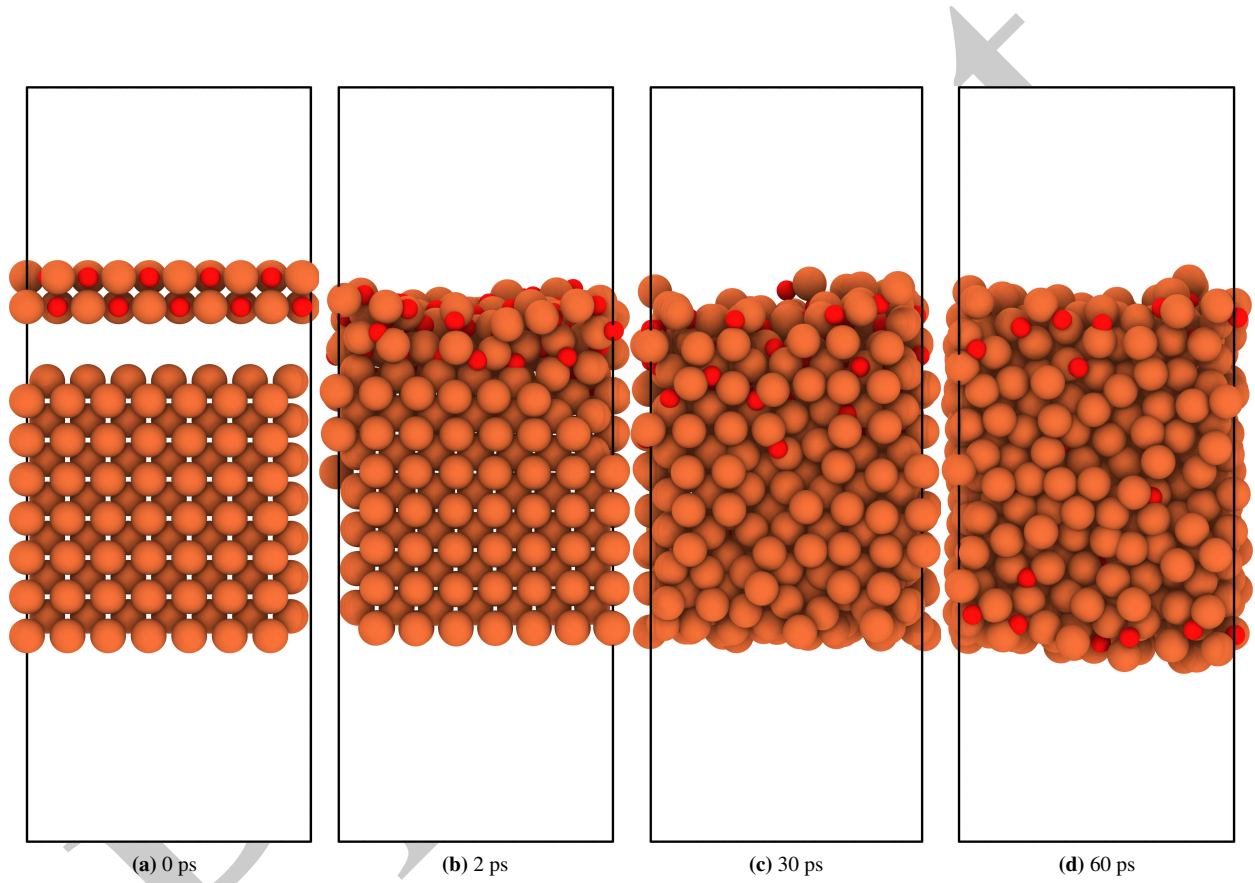
Figure 3: Realization of an iron-oxide surface with $Z_O = 0.11$ and $T_p = 2000$ K for different moments in time during the preparation phase with heating strategy 1. The figures show a lateral surface, with the top surface used for the scattering gas molecule. Red particles represent oxygen atoms, while the brown particles are iron atoms. The size of the particles equal the atomic radii.
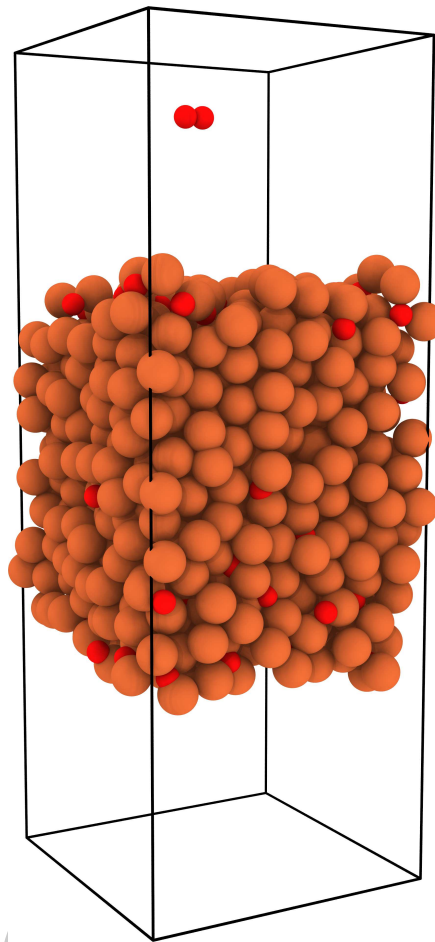
Figure 4: Initial configuration showing an oxygen molecule (red particles) placed above a partially oxidized iron surface (brown particles) with $Z_O = 0.11$ and $T_p = 2000$ K. The size of the particles equal the atomic radii.

A similar approach as Sipkens and Daun (2018) is used to evaluate the reactive force fields; the effect of the reactive force fields on the surface characteristics is investigated by examining the thermal expansion of iron oxides. Figure 5 shows the MD-derived densities of FeO and Fe_3O_4 as a function of the surface temperature. In this section, the definitions "liquid FeO" and "liquid Fe_3O_4" will be used again. The experimentally obtained densities of FeO (Lee and Gaskell, 1974, Saxena et al., 1993, Xin et al., 2019) and Fe_3O_4 (Hahn, 1984) are added as a reference. The density of liquid FeO is extrapolated based on the dV/dt expression stated in Table 4 of Xin et al. (2019). To the authors' knowledge, the density above the melting point of Fe_3O_4 is unavailable in literature. Therefore, the comparison for Fe_3O_4 is limited to the solid phase.

There is a clear difference between the MD-derived densities with ReaxFF FeOCHCl−2010 and ReaxFF FeCHO − 2016 for the density curves of FeO. The ReaxFF FeOCHCl − 2016 surface consistently underestimates densities and lacks a clear phase transition; the FeO surface resembles a liquid surface over the complete temperature range. The ReaxFF FeOCHCl − 2010 model matches the experimentally obtained values better, particularly in the solid phase, and there is a clear phase transition from solid to liquid.

The difference between ReaxFF FeOCHCl − 2010 and ReaxFF FeCHO − 2016 for the density curves of Fe_3O_4 is small. In the solid-phase regime, the density obtained with ReaxFF FeOCHCl − 2010 provides a better match. As a result, it could be concluded that ReaxFF FeOCHCl − 2010 is better suited to reproduce a FeO and Fe_3O_4 surface, and therefore, this reactive force field is used in this work.
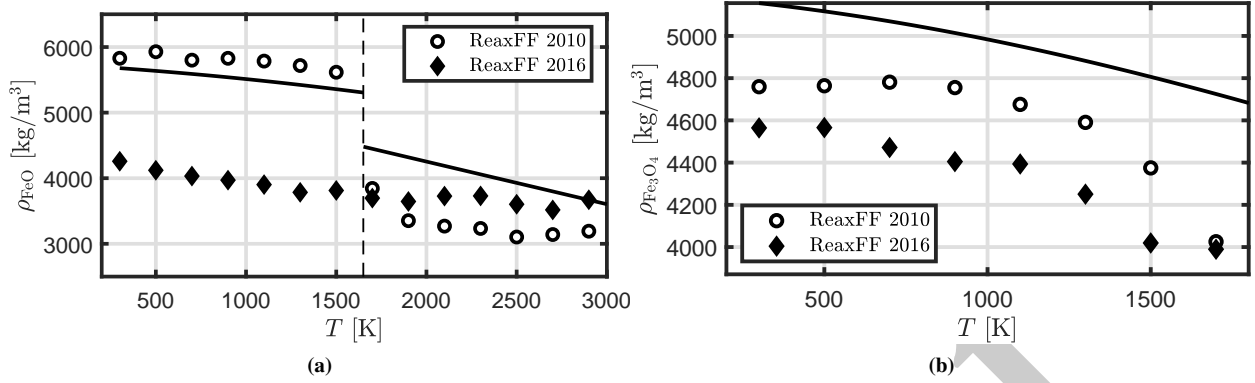
Figure 5: MD-derived density of FeO and Fe_3O_4 as a function of temperature for ReaxFF FeOCHCl $-$ 2010 (Aryanpour et al., 2010) with the ReaxFF FeCHO $-$ 2016 (Islam et al., 2016). Experimentally obtained values (solid line) are shown as a reference.
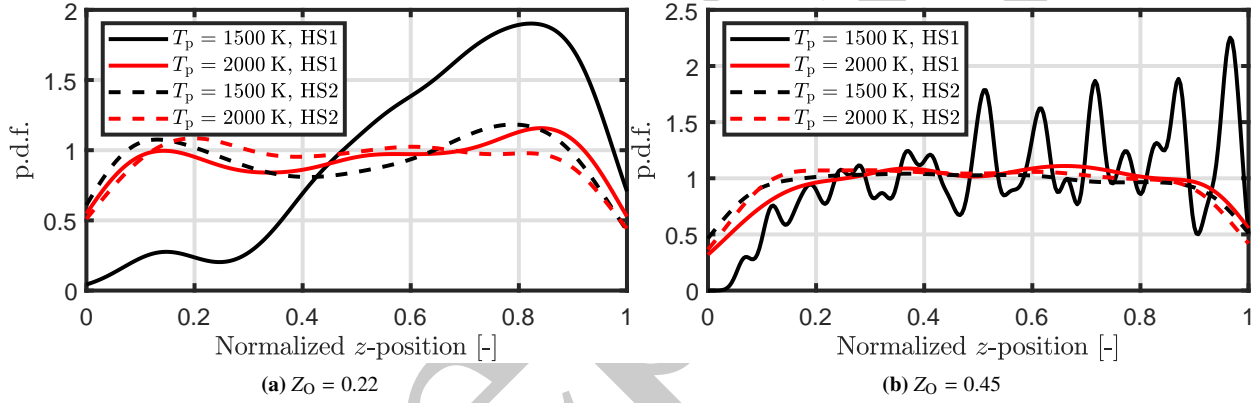

(a) $Z_O = 0.22$

(b) $Z_O = 0.45$

Figure 6: Probability density function of oxygen atoms z-position for two different heating strategies, T_p and Z_O.

4.2. Mass accommodation coefficients

The mass accommodation coefficient for iron with oxygen is investigated for different initial oxidation stages, ranging from $Z_O = 0$ to $Z_O = 0.57$, and three different surface temperatures, namely T_p = 1500, 2000 and 2500 K, of which the latter two are in the liquid-phase regime.

As discussed in Section 3.3, two different heating strategies are employed to investigate the effect of the non-uniform distribution of oxygen atoms in the surface. Figure 6 shows the probability density function of oxygen atoms z-position as a function of surface height for the two different heating strategies. For T_p = 2000 K, the oxygen atoms are characterized by a relatively uniform distribution, independent of the heating strategy. This lack of dependency is, however, not the case for T_p = 1500 K. With heating strategy 1 (HS1), the oxygen atoms are not uniformly distributed—a higher concentration is observed near the top surface. Because of the heating rate of HS1, not all of the oxygen atoms are sufficiently diffused to reach a uniform distribution. As a result, more oxygen atoms are near the surface. When the annealing process of HS2 is used, a spatially more uniform distribution of oxygen atoms is obtained.

Figure 7a shows the MAC of oxygen as a function of initial oxidation stage for the three different surface temperatures, obtained with HS2, while 7b shows a detailed view around $Z_O = 0.57$. To show the effect of a higher oxygen concentration at the top surface, the MAC obtained with HS1 for T_p = 1500 K is added as the red line. With a homogeneously distributed surface obtained via HS2, the MAC is barely depends on the surface temperature and decreases almost linearly as a function of Z_O. Two different slopes are observed, one steeper if Z_O < 0.5 and one shallower if Z_O > 0.5. When Z_O > 0.5, the MAC decreases with a different slope, indicating that once the particle
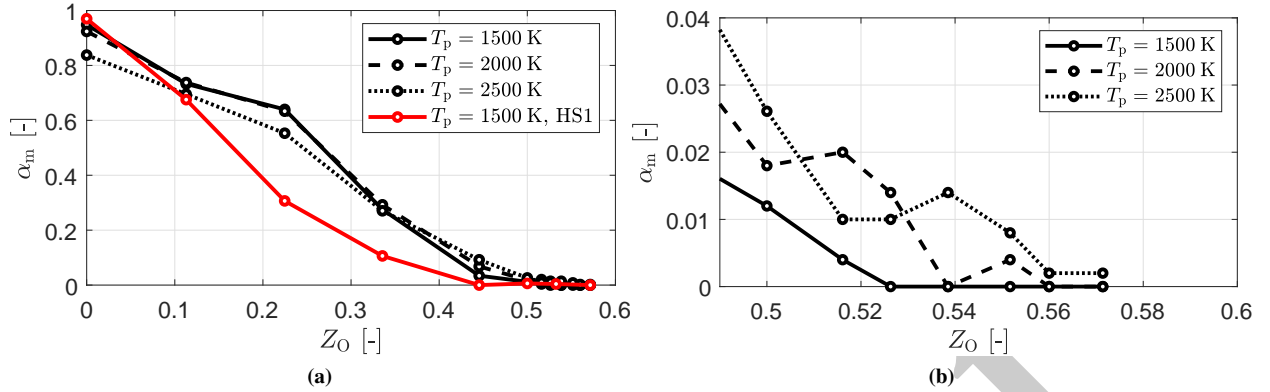
11

Figure 7: The mass accommodation coefficient of oxygen as a function of initial oxidation stage at three different surface temperatures. A detailed view around $Z_O = 0.5$ is shown in (b).

reaches stoichiometric FeO, it becomes more difficult to absorb oxygen. Figure 7b shows a detailed view of the MAC in the region $0.5 < Z_O < 0.57$. In this region, a more prominent effect of the surface temperature is observed—the MAC increases with an increasing surface temperature.

The effect of the non-uniform distribution of oxygen atoms on the MAC is shown in Figure 7a with the red line. The MAC decreases significantly if there are more oxygen atoms near the surface. This accumulation at the top surface prevents new oxygen atoms from being accommodated, indicating that the mass accommodation coefficient is affected by the local oxygen concentration near the surface. Therefore, if the iron particle does not have a spatially uniform composition, internal transport may limit the oxidation rate of iron particles.

4.3. Thermal accommodation coefficients

4.3.1. Fe - N_2 interactions

The TAC for the Fe - N_2 interaction is investigated for a smooth and rough surface. An initially rough surface was created by projecting iron atoms on the initial smooth lattice. Figure 8 shows the thermal accommodation coefficients of the Fe-N_2 interaction as a function of iron surface temperature for the two different surfaces. For the smooth surface, the TAC increases as a function of surface temperature from $\alpha_T = 0.08$ up to $\alpha_T = 0.19$. This trend is consistent with the values experimentally obtained by Sipkens et al. (2014), who reported a value of 0.10 and 0.17. The increasing TAC value can be attributed to the change of a relatively smooth surface in the solid phase into a rough surface in the liquid face when temperature increases (Sipkens and Daun, 2018). With a rough surface, the TAC values in the solid phase increase to $\alpha_T = 0.17$, almost independent of surface temperature. From the point where the iron surface becomes a liquid (1800 K), the difference between initially smooth and rough surfaces disappears.

In addition to the surface temperature of iron, the temperature of the surrounding gas can change significantly during iron combustion. Daun (2009) and Mane et al. (2018) investigated the effect of gas temperature on the TAC of nitrogen with soot and hydrogen with aluminum, respectively. They showed that the TAC is almost independent of gas temperature and primarily influenced by surface roughness and gas molecular weight. Based on the MD results, a recommended value for the TAC of the interaction between Fe with N_2 equals 0.17.

4.3.2. Fe_xO_y - O_2 interactions

The oxygen molecules that do not stick to the surface during Fe_xO_y-O_2 interactions still contribute to the TAC. Figure 9 shows the total thermal accommodation coefficients of the Fe_xO_y-O_2 interaction as a function of Z_O at three different surface temperatures. When the oxidation degree of the surface is low, the TAC remains close to unity but decreases sharply to 0.2 once $Z_O > 0.5$. Note that, if Z_O is small, and thus MAC is large, the amount of scattered oxygen atoms over which the TAC is calculated is low. Since the total thermal accommodation coefficient is calculated with Equation (21), however, this uncertainty in the low Z_O regime could be neglected due to the small contribution of α_{T,O_2} given by the large MAC number.
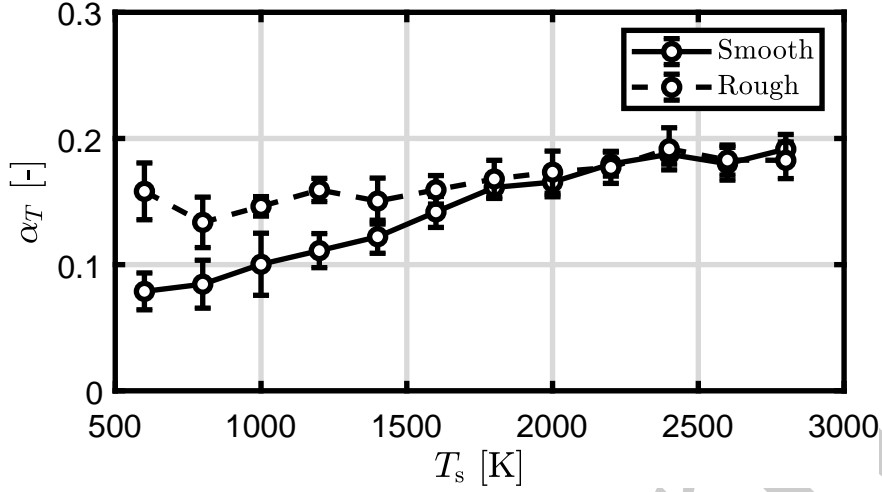
12

Figure 8: Total thermal accommodation coefficients of the Fe-N_2 interaction as a function of surface temperature for smooth and rough iron surfaces.
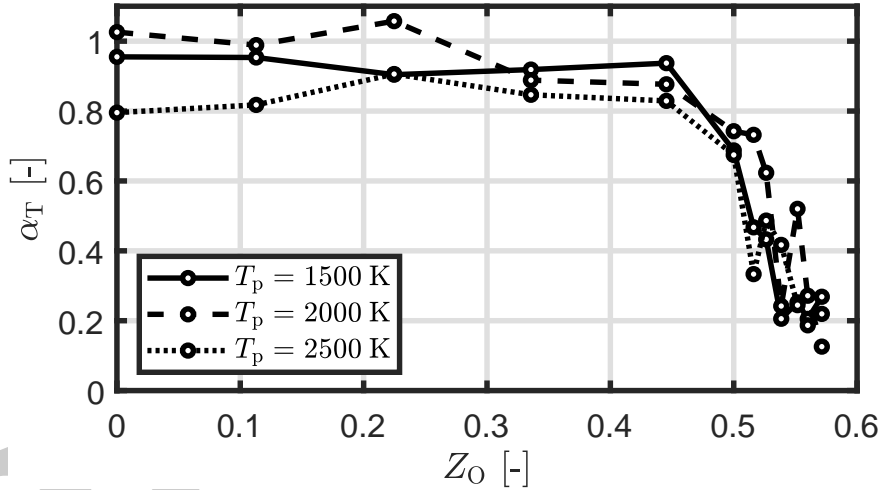

Figure 9: Total thermal accommodation coefficients of the Fe_xO_y-O_2 interaction as a function of Z_O at three different surface temperatures.

4.4. Discussion of the MD results

A limitation of the above molecular beam approach to determine the TAC and MAC is the assumption of a clean surface. Within experiments, surfaces could be (partly) covered by a layer of gas molecules. Song and Yovanovich (1987) proposed a semi-empirical correlation for the TAC of engineering surfaces, which takes into account this absorded layer. They state that the correlation is general and can be used for any combination of gases with a solid surface, in a wide temperature range. The correlation of Song and Yovanovich (1987) is also used in the work of Jean-Philyppe et al. (2022) to investigate the effect of the Knudsen transition regime on the i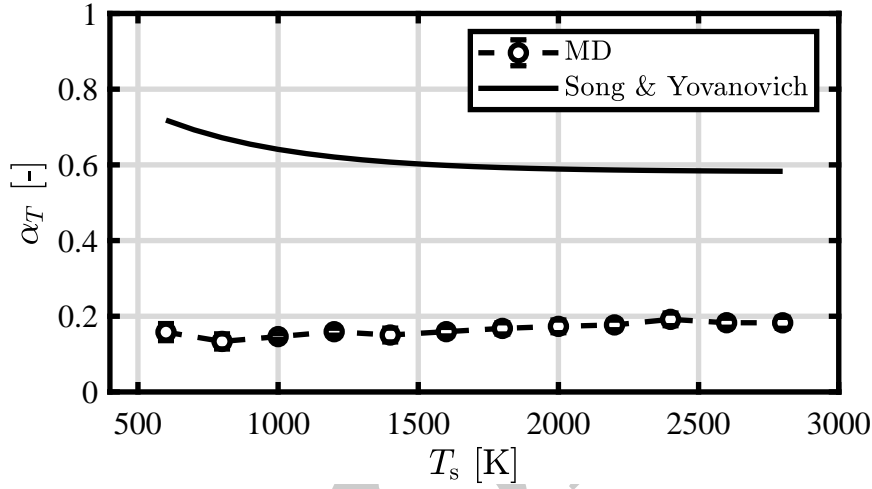gnition of single iron particles. Figure 10 shows the comparison between the TAC of the Fe-N_2 interaction obtained with the MD simulations compared to the semi-empirical correlation of Song and Yovanovich (1987). While Song and Yovanovich (1987) do not claim that the correlation is also valid in the liquid phase regime, their curve is extrapolated in the liquid phase regime for comparison with the MD results. It can be seen that the TAC of Song and Yovanovich (1987) is about three times larger than the TAC obtained with the molecular beam approach. However, Song and Yovanovich (1987) state that a common strategy to create an adsorption-free surface within experiments is to heat the surface to high temperatures above, 1000 K, to desorb all of the impurities in the surface. This work is mainly focused on the accommodation

Table 1: TAC and MAC for the Fe_xO_y - O_2 interactions, averaged over the three phase temperatures.

Z_O	0	0.11	0.22	0.34	0.45	0.5	0.52	0.53	0.54	0.55	0.56	0.57
α_m	0.902	0.730	0.609	0.285	0.063	0.018	0.011	0.008	0.005	0.003	0.001	0.001
α_T	0.796	0.832	0.934	0.821	0.831	0.629	0.344	0.482	0.405	0.2510	0.190	0.221

coefficients in the liquid-phase regime. Since the current MD simulations better represent the condition of a liquid-phase surface rather than a solid-phase surface with intrinsic roughness, the resulting accommodation coefficients in the temperature range above the melting points are likely more accurate.

Figure 10: Thermal accommodation coefficients of the Fe-N_2 interaction obtained with the MD simulations compared to the semi-empirical correlation of Song and Yovanovich (1987).

Nejad et al. (2020) performed molecular dynamics simulations to investigate the influence of gas-wall and gas-gas interaction on different accommodation coefficients. They used a parallel wall approach to determine the accommodation coefficients, which means that an intermediate Knudsen number is modeled. They showed that using a molecular beam approach results in lower TAC values with respect to the parallel wall approach. In the case of a molecular beam approach, the effect of gas-gas interactions is neglected, which has an effect in the Knudsen transition regime. They showed that the TAC could be around 1.5 times larger if this effect were included. However, in the two-layer model used in this work, a free-molecular regime is assumed within the Knudsen layer, implying that each incoming gas molecules do not interact with each other. Therefore, the accommodation coefficients obtained via a molecular beam approach are consistent with the used two-layer model.

4.5. Implementation of the MD results in the single iron particle combustion model

The TAC and MAC obtained from the MD simulations are used in the single iron particle combustion model. In the iron particle model, it is assumed that the particle has a homogeneous mixture, such that there is no internal gradient in oxygen concentration. Therefore, the TAC and MAC values for Fe_xO_y-O_2 interactions are used from HS2, which are a function of Z_O and nearly independent of the surface temperature. In Table 1 the TAC and MAC for the Fe_xO_y - O_2 interactions are listed and averaged over the three surface temperatures. Within the iron particle combustion model, these values are used for linear interpolation. However, if no further oxidation is modeled after reaching the stoichiometry of FeO, a linear fit is used for the MAC such that $\alpha_m = 0$ if $Z_O = 0.5$. Equation (21) describes the total TAC with $\alpha_{T,N_2} = 0.17$ and $\alpha_{T,O_2} = f(Z_O)$.
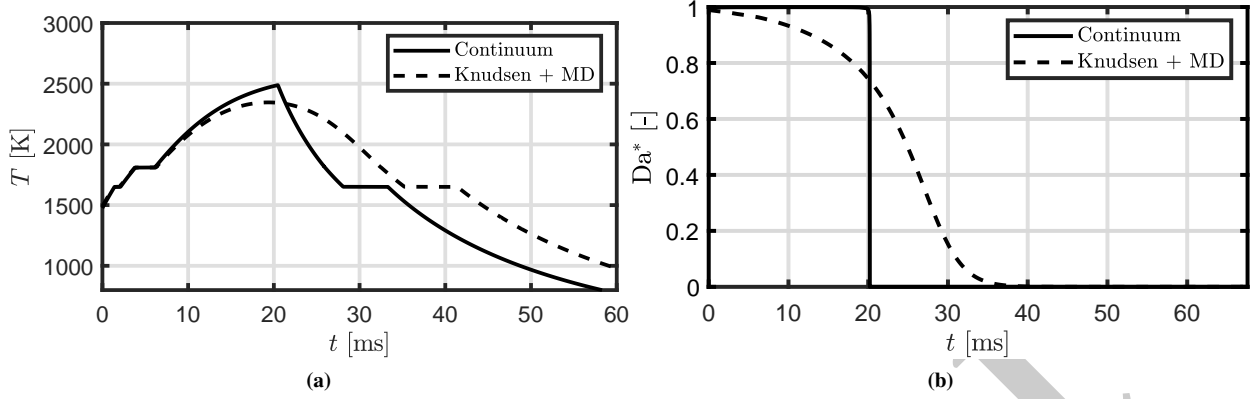
Figure 11: (a) Temperature profile and (b) normalized Damköhler number for an iron particle of 50 μm burning at 21% oxygen concentration. The continuum model is compared to the MD-informed Knudsen model.

5. Results of single iron particle combustion simulations

In this section, the results of the MD-informed Knudsen model for a single iron particle burning in an O_2-N_2 atmosphere are presented. An initial particle temperature just above the ignition temperature (Mi et al., 2022), $T_{p,0} = 1100$ K, is considered.

5.1. Combustion behavior

First, the effect of the new model by only considering the first oxidation stage up to $Z_O = 0.5$ is investigated. The initial conditions are chosen such that the laser-ignited experiments performed by Ning et al. (2021a) are mimicked. A cold gas of $T_{g,0} = 300$ K at 1 atm is considered. The temperature profiles are shifted such that the particle temperature equals $T_{p,0} = 1500$ K at $t = 0$ ms (Ning et al., 2021b).

Figure 11a shows the comparison of the temperature profiles between the continuum model and the MD based Knudsen model for a 50 μm particle burning in $X_{O_2} = 0.21$. The temperature *vs.* time curve for the MD-informed Knudsen model changes significantly compared to the previously used continuum model. This difference can be explained by examining the Z_O value and heat transfer rates plotted in Figure 12. In the continuum model, the maximum temperature was located at the position where $Z_O = 0.5$ is reached. At that time, the available iron is completely oxidized, and therefore the heat release rate immediately drops to zero. With the MD based Knudsen model this behavior changes, and $Z_O = 0.5$ is reached after the peak temperature. Since the rate of oxidation slows down, as the MAC decreases with an increasing oxidation stage, the rate of heat loss exceeds the rate of heat release upon reaching the maximum temperature of the particle.

With the continuum model, it was discussed that the particle burns in a regime limited by the external diffusion of oxygen up to the maximum temperature. One can derive a normalized Damköhler number Da*. If Da* is close to zero, the particle burns in a kinetic- (or chemical-) absorption-limited regime, and if it is close to unity, the particle burns in an external-diffusion-limited regime. Figure 11b shows the normalized Damköhler number for the same configuration. The normalized Damköhler number of the continuum model is determined according to the definition of Hazenberg and van Oijen (2021). For the Knudsen + MD model, the normalized Damköhler number is defined as

$$Da^* = 1 - \frac{\alpha_m X_{O_2,\delta}}{X_{O_2,g}}, \tag{27}$$

where $\alpha_m X_{O_2,\delta}$ denotes the molar fraction of oxygen at the particle surface $X_{O_2,p}$. As discussed before, with the continuum model the particle burns purely in an external-diffusion-limited regime up to the maximum temperature. This behavior changes in the MD-informed Knudsen model: Due to the decreasing MAC value with an increasing oxidation stage, the particle burns in an intermediate regime.
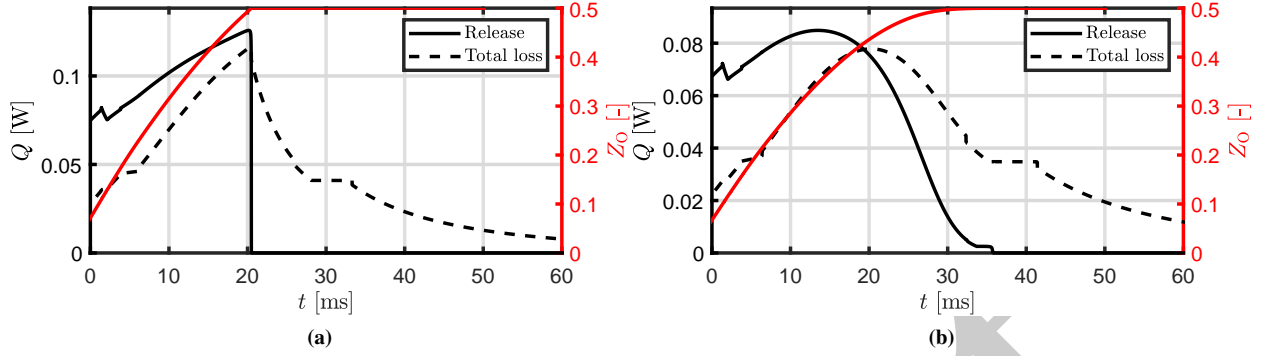
15

Figure 12: Heat release and heat loss rates (left axis) and Z_O (right axis) for an iron particle of 50 μm burning at 21% oxygen concentration. The results are shown for (a) the continuum model and (b) the MD-informed Knudsen model.
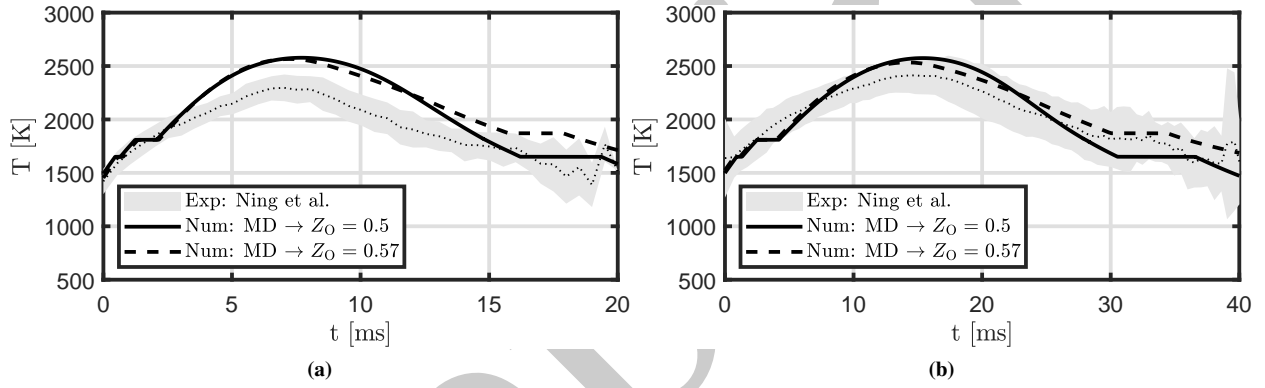

Figure 13: Temperature profile for an iron particle of (a) 34 μm and (b) 50 μm burning at 26% oxygen concentration, with and without further oxidation beyond $Z_O = 0.5$. The dotted line and gray area are the mean and standard deviation of measurements obtained with the setup of Ning et al. (2021a), respectively.

5.2. Comparison with experimental results

In Thijs et al. (2022, 2023), only the first stage of combustion, which is the conversion from up to $Z_O = 0.5$, was investigated. Due to this assumption, an inert cooling stage was observed after the peak temperature. However, Choisez et al. (2022) investigated combusted iron powders and discovered that it primarily consisted of a magnetite and hematite mixture, indicating a Z_O greater than 0.5. With the MD-informed Knudsen model, the oxidation beyond $Z_O = 0.5$ can be included in the combustion of a single particle.

The results of the MD-informed Knudsen model are compared with two sets of experimental data. First, the model is compared to the laser-ignited experiments of Ning et al. (2021b) wherein the particles burn in air at 300 K. Then, the new temperature curve is compared to the drop-tube experiments of Panahi et al. (2022) wherein the particles burn in varying oxygen concentrations at 1350 K. The experimental data are averaged over multiple independent single-particle measurements to obtain a smooth curve.

5.2.1. Comparison with Ning et al.

Figure 13 shows the temperature profiles for the MD-informed Knudsen model with and without further oxidation beyond $Z_O = 0.5$ for a 34 μm and 50 μm particle burning in air with $X_{O_2} = 0.26$. The dotted line and gray area in Figure 13 are the mean and standard deviation of the experimentally obtained temperature profiles, respectively.

The particle temperature for smaller particles is overestimated is overestimated. Overall, the temperature curve obtained with the MD-informed Knudsen model shows a better agreement with the experimentally obtained temperature curve than the continuum-model prediction. The sharp transition at the peak temperature is now a smooth curve.
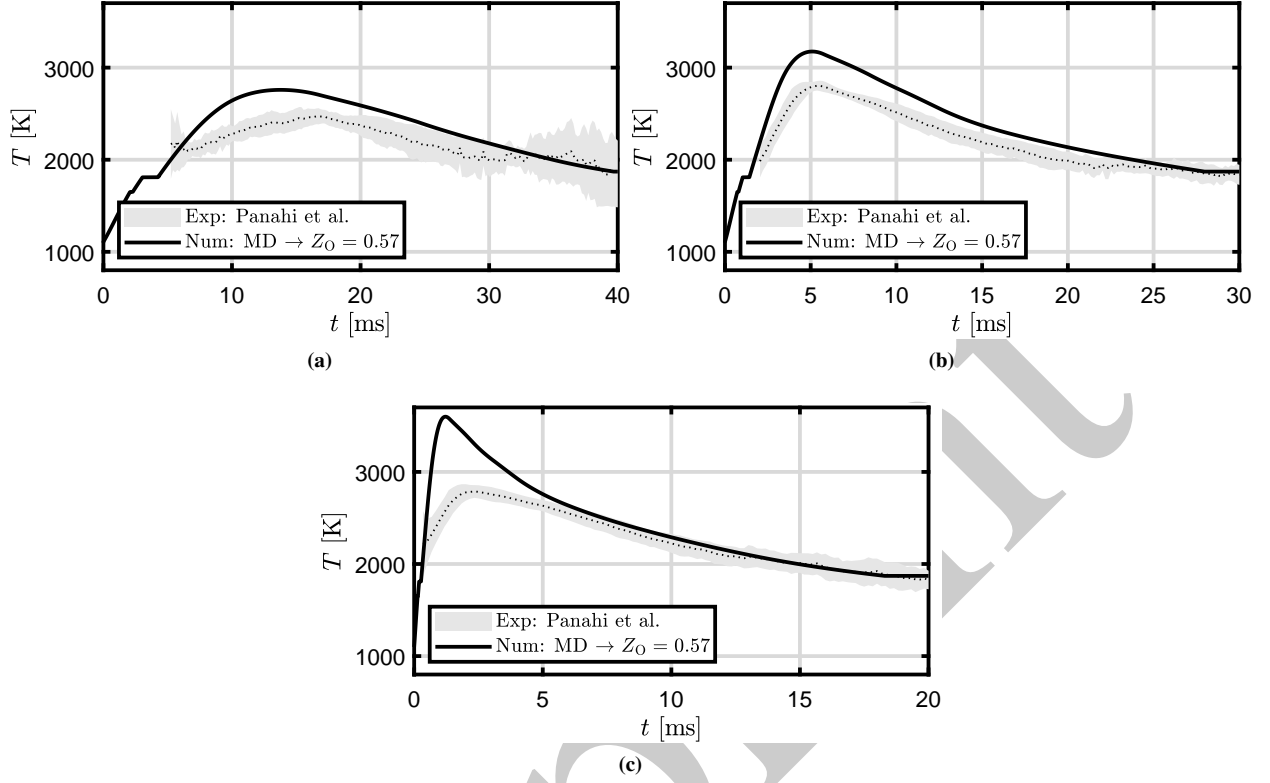
Figure 14: Temperature profile for an iron particle of 49 μm burning at (a) 21%, (b) 50% and (c) 99 % oxygen concentration. The dotted line and gray area are the mean and standard deviation of measurements obtained with the setup of Panahi et al. (2022), respectively.

The inclusion of the oxidation above $Z_O = 0.5$ results in a higher temperature in the tail of the curve. Instead of inert cooling after $Z_O = 0.5$, a reactive cooling regime is observed. The new numerically obtained slopes after the peak temperature qualitatively better agree with the experimental measurement during the cooling stage.

5.2.2. Comparison with Panahi et al.

Figure 14 shows the temperature profiles for the MD-informed Knudsen model with further oxidation beyond $Z_O = 0.5$ for a 49 μm particle burning in air with $X_{O_2} = 0.21$, 0.5 and 0.99. The dotted line and gray area are the mean and standard deviation of experimentally obtained temperature profiles, respectively, which are calculated via the setup described by Panahi et al. (2022). Note that the effect of the Stefan flow correction on the evaporation rate is not taken into account. The data of Panahi et al. (2022) are time-shifted so that the first experimental data point approximates the numerical temperature.

Although the model overestimates the particle temperature at the two higher oxygen concentrations, the agreement after the maximum temperature is reasonable. The reactive cooling slope which is observed after the maximum particle temperature seems to match the experimentally observed slope. This qualitative agreement implies that the particle keeps on oxidizing after the maximum particle temperature is reached.

A possible explanation for the overestimation of the particle temperature at higher oxygen concentrations could be due to assume infinitely fast internal transport for these high oxygen concentrations. As shown in Section 4.2, the mass accommodation coefficient significantly decreases when the particle does not have a homogeneous composition, but a higher concentration of oxygen atoms near the surface. Since for high oxygen concentrations in the gas, the external diffusion of oxygen is fast, the diffusion of oxygen in the condensed phase could be rate-limiting. With an increasing oxidation stage Z_O, and an increased oxygen concentration X_{O_2} in the gas phase, internal transport could limit the absorption rate of new oxygen molecule, and therefore limit the maximum particle temperature.
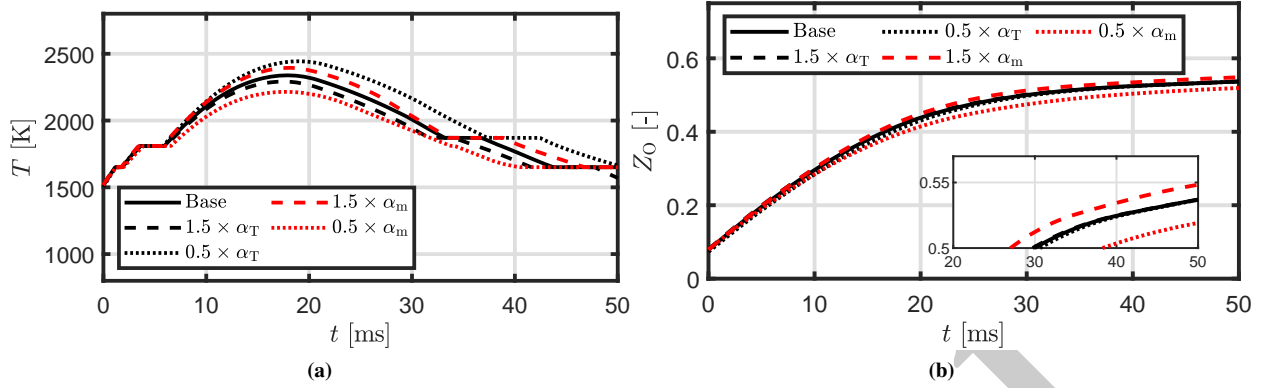
Figure 15: The effect of changes in α_T and α_m for a iron particle of 50 μm burning at 21% oxygen concentration. (a) The particle temperature and (b) Z_O.

5.3. Effect of α_T and α_m

The results of the molecular dynamics simulations are dependent on the accuracy of the inter-atomic potentials and, perhaps, also on the configuration. Related changes in the TAC and MAC have an effect on the temperature profile during combustion. In this section, the TAC and MAC are varied independently in the Knudsen model to investigate the effect on the combustion behavior.

The MD-informed TAC and MAC are varied by 50%, with a maximum value of 1. Figure 15 shows the effect on the temperature profile and Z_O for a 50 μm particle burning in $X_{O_2} = 0.21$. Both α_T and α_m have a significant effect on the particle temperature. The maximum temperature could vary by 150 K due to the variations of α_T and α_m.

An increasing α_T results in a lower particle temperature, while the opposite is seen for a decreasing α_T. With an increasing α_T, the exchange of kinetic energy between the gas molecules and the surface is more efficient, resulting in a greater rate of heat loss and therefore a decreasing particle temperature. A variation in α_T hardly affects the oxidation rate.

A variation in α_m affects both the temperature profile as well as the oxidation stage Z_O. An increasing α_m results in a faster oxidation rate for the iron particle, leading to a faster heat release and therefore an increase in particle temperature. Note that the variation is relative, and thus the absolute difference with respect to the original values becomes less when α_m is close to zero.

5.4. Effect of transition modeling

The effect of the transition regime on the temperature profile of a variety of particles burning in $X_{O_2} = 0.21$ is investigated finally. Figure 16 shows the difference for the time to maximum temperature t_{max} and the maximum temperature T_{max} obtained with either the continuum and transition model as a function of particle diameter. Due to the large difference in values for t_{max}, the relative difference with respect to the continuum model is plotted, while for the maximum temperature two separate curves are plotted. The error bars show the effect of varying both α_T and α_m by 50 %.

When using the MD-informed Knudsen model, it is clear that the time to maximum temperature increases for smaller particles. Since the free-molecular regime inhibits mass transfer towards the particle, t_{max} increases. However, with an increasing particle size, the new t_{max} value becomes smaller than with the continuum model. This result is recognized as an effect of the decreasing MAC with an increasing Z_O.

T_{max} as a function of particle size also changes with respect to the continuum model. It is hard to distinguish any transition regime effects in this curve since due to the decreasing MAC with increasing Z_O, the maximum temperature already decreased with respect to the continuum model. Ning et al. (2021b) observed a decreasing maximum particle temperature with a decreasing particle size in the range of 25-54 μm. However, this trend is still not observed in the numerical model, and can therefore not be explained by the effect of the transition-regime heat and mass transfer.

A critical diameter $d_{p,c}$ is defined, which means that if $d_p < d_{p,c}$, it is important to include the transition regime. For $d_{p,c}$ we define that If one considers $t_{max}/t_{max,co} < 1.10$ as the criterion, critical particle size is found to be $d_{p,c} \approx 10$ μm.
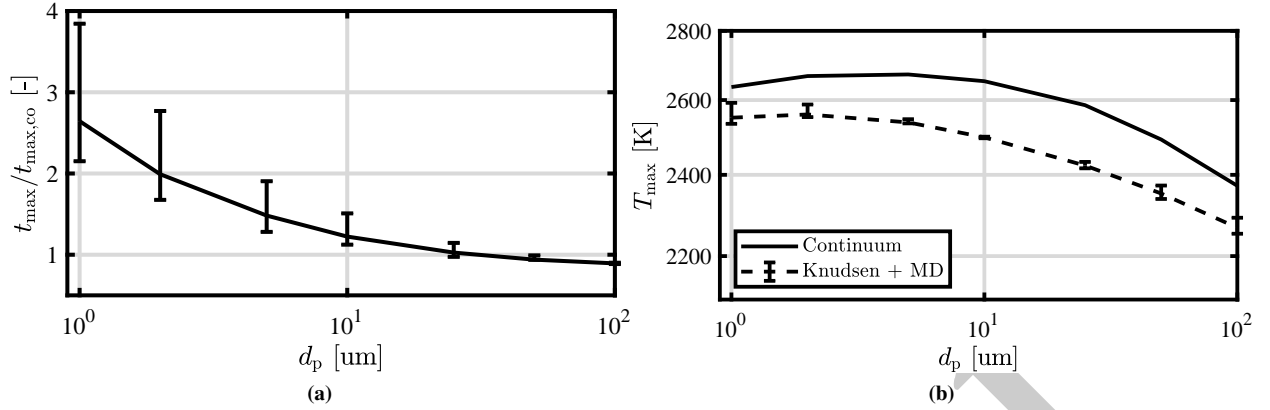
18

Figure 16: The effect of the MD-informed Knudsen model compared to the continuum model with (a) $t_{max}/t_{max,co}$ and (b) T_{max}. Values are obtained with $X_{O_2} = 0.21$.

This criterion suggests that, if one uses a continuum-based model to describe the combustion of iron particles smaller than 10 μm, the burn time can be underestimated by more than 10% due to neglecting the effects of transition-regime transport phenomena.

6. Conclusions

Molecular dynamics simulations have been performed to investigate the thermal and mass accommodation co-efficients for the combination of iron(-oxide) and air. The obtained relations for the TAC and MAC are used in a point-particle Knudsen model to investigate the effects on the combustion behavior of (fine) iron particles.

The TAC for the interaction of Fe with N_2 is almost independent of the surface temperature and equals $\alpha_T = 0.17$. For Fe_xO_y-O_2 interactions, the TAC remains close to unity when the oxidation degree of the surface is low, but decreases abruptly to 0.2 once it reaches the stoichiometry of FeO. The MAC decreases almost linearly as a function of Z_O. Two different slopes are observed: A steeper slope for $Z_O < 0.5$ and a shallower one for $Z_O > 0.5$, indicating that it becomes more difficult for an iron(-oxide) particle to absorb more oxygen for $Z_O > 0.5$.

By incorporating the MD information into the single iron particle model, a new temperature-time curve for the single iron particles is observed compared to results obtained with previously developed continuum models. Since the rate of oxidation slows down as the MAC decreases with an increasing oxidation stage, the rate of heat release decreases when reaching the maximum temperature, such that the rate of heat loss exceeds that of heat release. In addition, the oxidation beyond $Z_O = 0.5$ (from stoichiometric FeO to Fe_3O_4) is modeled. The effect of the transition-regime heat and mass transfer on the burn time becomes more than 10% if the particles are smaller than 10 μm.

In some cases, the model overestimates the particle temperature. The reactive cooling slope observed after the maximum particle temperature, however, reasonably agree with the experimentally observed slope. This overestimation could be attributed to the assumption of an infinitely fast transport of oxygen inside the particle. If the particle does not have a homogeneous composition, the mass accommodation coefficient significantly decreases. With a high oxygen concentration X_{O_2} in the gas phase, the rate of internal transport could become important, and therefore limit the maximum temperature.

7. Acknowledgements

References

Aryanpour, M., van Duin, A.C.T., Kubicki, J.D., 2010. Development of a reactive force field for Iron-Oxyhydroxide systems. J. Phys. Chem. A. 114, 6298–6307. doi:10.1021/jp101332k. pMID: 20455552.

Bergthorson, J.M., Goroshin, S., Soo, M.J., Julien, P., Palecka, J., Frost, D.L., Jarvis, D.J., 2015. Direct combustion of recyclable metal fuels for zero-carbon heat and power. Appl. Energy 160, 368–382.

Choisez, L., van Rooij, N.E., Hessels, C.J., da Silva, A.K., Filho, I.R.S., Ma, Y., de Goey, P., Springer, H., Raabe, D., 2022. Phase transformations and microstructure evolution during combustion of iron powder. Acta Materialia 239, 118261.

Daun, K., 2009. Thermal accommodation coefficients between polyatomic gas molecules and soot in laser-induced incandescence experiments. Int. J. Heat Mass Transf. 52, 5081–5089. doi:https://doi.org/10.1016/j.ijheatmasstransfer.2009.05.006.

Daun, K., Titantah, J., Karttunen, M., 2012. Molecular dynamics simulation of thermal accommodation coefficients for laser-induced incandescence sizing of nickel particles. Appl. Phys. B 107, 221–228. doi:https://doi.org/10.1007/s00340-012-4896-x.

van Duin, A.C.T., Dasgupta, S., Lorant, F., Goddard, W.A., 2001. ReaxFF: a reactive force field for hydrocarbons. J. Phys. Chem. A 105, 9396–9409. doi:10.1021/jp004368u.

van Gool, C.E.A.G., Thijs, L.C., Ramaekers, W.J.S., Kuerten, J.G.M., van Oijen, J.A., de Goey, L.P.H., 2022. Particle equilibrium composition model for iron dust combustion. Prog. Energy Combust. (under review) .

Hahn, T.A., 1984. Thermal expansion 8 .

Hazenberg, T., van Oijen, J.A., 2021. Structures and burning velocities of flames in iron aerosols. Proc Combust Inst. 38, 4383–4390.

Islam, M.M., Zou, C., van Duin, A.C.T., Raman, S., 2016. Interactions of hydrogen with the iron and iron carbide interfaces: a ReaxFF molecular dynamics study. Phys. Chem. Chem. Phys. 18, 761–771. doi:10.1039/C5CP06108C.

Jean-Philyppe, J., Fujinawa, A., Bergthorson, J., Mi, X., 2022. The ignition of fine iron particles in the knudsen transition regime doi:10.13140/RG.2.2.30880.05129.

Kritikos, E., Lele, A., van Duin, A.C., Giusti, A., 2022. A reactive molecular dynamics study of the effects of an electric field on n-dodecane combustion. Combust Flame 244, 112238.

Lee, Y.E., Gaskell, D.R., 1974. The densities and structures of melts in the system CaO-"FeO"-SiO$_2$. Metall. Mater. Trans. B 5, 853–860.

Li, S., Huang, J., Weng, W., Qian, Y., Lu, X., Aldén, M., Li, Z., 2022. Ignition and combustion behavior of single micron-sized iron particle in hot gas flow. Combustion and Flame 241. doi:10.1016/j.combustflame.2022.112099.

Li, S., Sanned, D., Huang, J., Berrocal, E., Cai, W., Aldén, M., Richter, M., Li, Z., 2021. Stereoscopic high-speed imaging of iron microexplosions and nanoparticle-release. Opt. Express 29, 34465–34476.

Liu, F., Daun, K.J., Snelling, D.R., Smallwood, G.J., 2006. Heat conduction from a spherical nano-particle: status of modeling heat conduction in laser-induced incandescence. Appl. Phys. B 83, 355–382.

Mane, T., Bhat, P., Yang, V., Sundaram, D.S., 2018. Energy accommodation under non-equilibrium conditions for aluminum-inert gas systems. Surf Sci. 677, 135–148. doi:https://doi.org/10.1016/j.susc.2018.05.011.

McRae, M., Julien, P., Salvo, S., Goroshin, S., Frost, D.L., Bergthorson, J.M., 2019. Stabilized, flat iron flames on a hot counterflow burner. Proc. Combust. Inst. 37, 3185–3191. doi:https://doi.org/10.1016/j.proci.2018.06.134.

Mi, X., Fujinawa, A., Bergthorson, J.M., 2022. A quantitative analysis of the ignition characteristics of fine iron particles. Combustion and Flame 240, 112011.

Nejad, S.M., Nedea, S., Frijns, A., Smeulders, D., 2020. The influence of gas–wall and gas–gas interactions on the accommodation coefficients for rarefied gases: A molecular dynamics study. Micromachines 11.

Ning, D., Shoshin, Y., van Oijen, J.A., Finotello, G., de Goey, L.P.H., 2021a. Burn time and combustion regime of laser-ignited single iron particle. Combust. Flame 230, 111424.

Ning, D., Shoshin, Y., van Stiphout, M., van Oijen, J.A., Finotello, G., de Goey, L.P.H., 2021b. Temperature and phase transitions of laser ignited single iron particle. Combust. Flame 236, 111801.

Panahi, A., Chang, D., Schiemann, M., Fujinawa, A., Mi, X., Bergthorson, J.M., Levendis, Y.A., 2022. Combustion behavior of single iron particles–part i: An experimental study in a drop-tube furnace under high heating rates and high temperatures. Applications in Energy and Combustion Science , 100097.

Saxena, S.K., Chatterjee, N., Fei, Y., Shen, G., 1993. Thermodynamic Data on Oxides and Silicates. 1 ed., Springer-Verlag Berlin Heidelberg.

Senyurt, E.I., Dreizin, E.L., 2022. At what ambient temperature can thermal runaway of a burning metal particle occur? Combust. Flame 236, 111800. doi:https://doi.org/10.1016/j.combustflame.2021.111800.

Sipkens, T.A., Daun, K.J., 2018. Effect of surface interatomic potential on thermal accommodation coefficients derived from molecular dynamics. J. Phys. Chem. C. 122, 20431–20443. doi:10.1021/acs.jpcc.8b06394.

Sipkens, T.A., Singh, N.R., Daun, K.J., Bizmark, N., Ioannidis, M., Titantah, J.T., Karttunen, M., 2014. Time resolved laser induced incandescence for sizing aerosolized iron nanoparticles Volume 8B: Heat Transfer and Thermal Engineering. doi:10.1115/IMECE2014-38515.

Song, S., Yovanovich, M.M., 1987. Correlation of thermal accommodation coefficient for engineering surfaces. ASME HTD 69, 107–116.

Soo, M., Mi, X., Goroshin, S., Higgins, A.J., Bergthorson, J.M., 2018. Combustion of particles, agglomerates, and suspensions – a basic thermo-physical analysis. Combust. Flame. 192, 384–400.

Soo, M.J., Kumashiro, K., Goroshin, S., Frost, D.L., Bergthorson, J.M., 2017. Thermal structure and burning velocity of flames in non-volatile fuel suspensions. Proc. Combust. Inst. 36, 2351–2358. doi:https://doi.org/10.1016/j.proci.2016.06.043.

Srinivasan, S.G., van Duin, A.C.T., Ganesh, P., 2015. Development of a ReaxFF potential for carbon condensed phases and its application to the thermal fragmentation of a large fullerene. The Journal of Physical Chemistry A 119, 571–580.

Tang, F.D., Goroshin, S., Higgins, A., Lee, J., 2009. Flame propagation and quenching in iron dust clouds. Proc. Combust. Inst. 32, 1905–1912. doi:https://doi.org/10.1016/j.proci.2008.05.084.

Thijs, L.C., van Gool, C.E.A.G., Ramaekers, W.J.S., Kuerten, J.G.M., van Oijen, J.A., de Goey, L.P.H., 2022. Improvement of heat- and mass transfer modeling for single iron particles combustion using resolved simulations. Combust Sci Technol. 0, 1–17. doi:10.1080/00102202.2022.2089030.

20

Thijs, L.C., van Gool, C.E.A.G., Ramaekers, W.J.S., van Oijen, J.A., de Goey, L.P.H., 2023. Resolved simulations of single iron particle combustion and the release of nanoparticles. Proc Combust Inst. doi:10.1016/j.proci.2022.07.044.

Thompson, A.P., Aktulga, H.M., Berger, R., Bolintineanu, D.S., Brown, W.M., Crozier, P.S., in 't Veld, P.J., Kohlmeyer, A., Moore, S.G., Nguyen, T.D., Shan, R., Stevens, M.J., Tranchida, J., Trott, C., Plimpton, S.J., 2022. LAMMPS - a flexible simulation tool for particle-based materials modeling at the atomic, meso, and continuum scales. Comp. Phys. Comm. 271, 108171. doi:10.1016/j.cpc.2021.108171.

Tóth, P., Ögren, Y., Sepman, A., Gren, P., Wiinikka, H., 2020. Combustion behavior of pulverized sponge iron as a recyclable electrofuel. Powder Technol. 373, 210–219.

Wriedt, H.A., 1991. The Fe-O (iron-oxygen) system. Journal of Phase Equilibria 12, 170–200.

Xin, J., Gan, L., Wang, N., Chen, M., 2019. Accurate density calculation for molten slags in SiO2-Al2O3-CaO-MgO-'FeO'-'Fe2O3'. Metall. Mater. Trans. B 50, 2828–2842.

Yan, H.J., Zhuang, J.C., Zhou, P., Li, Q., Zhou, C.Q., Fu, P., 2017. Molecular dynamics simulation of thermal physical properties of molten iron. Int. J. Heat Mass Transf. 109, 755–760. doi:https://doi.org/10.1016/j.ijheatmasstransfer.2017.02.027.

Zhou, X.W., Johnson, R.A., Wadley, H.N.G., 2004. Misfit-energy-increasing dislocations in vapor-deposited CoFe/NiFe multilayers. Phys. Rev. B 69, 144113. doi:10.1103/PhysRevB.69.144113.

Zou, C., van Duin, A.C.T., Sorescu, D.C., 2012. Theoretical investigation of hydrogen adsorption and dissociation on iron and iron carbide surfaces using the ReaxFF reactive force field method. Top. Catal 55, 391–401.